INTERNATIONAL JOURNAL FOR NUMERICAL METHODS IN FLUIDS
Int. J. Numer. Meth. Fluids 2000; **33**: 279–312

Natural convection in porous media—dual reciprocity boundary element method solution of the Darcy model

Božidar Šarler[a,*], Dominique Gobin[b], Benoît Goyeau[b], Janez Perko[a] and Henry Power[c,d]

[a] *Laboratory for Fluid Dynamics and Thermodynamics, Faculty of Mechanical Engineering, University of Ljubljana, Ljubljana, Slovenia*
[b] *Laboratoire FAST, UMR CNRS 7608, Bât. 502, Campus Universitaire, Orsay, France*
[c] *Wessex Institute of Technology, Ashurst Lodge, Ashurst, Southampton, U.K.*
[d] *Instituto de Mecanica de Fluidos, Universidad Central de Venezuela, Caracas, Venezuela*

SUMMARY

This paper describes the solution of a steady state natural convection problem in porous media by the dual reciprocity boundary element method (DRBEM). The boundary element method (BEM) for the coupled set of mass, momentum, and energy equations in two dimensions is structured by the fundamental solution of the Laplace equation. The dual reciprocity method is based on augmented scaled thin plate splines. Numerical examples include convergence studies with different mesh size, uniform and non-uniform mesh arrangement, and constant and linear boundary field discretizations for differentially heated rectangular cavity problems at filtration with Rayleigh numbers of $Ra^* = 25$, 50, and 100 and aspect ratios of $A = 1/2$, 1, and 2. The solution is assessed by comparison with reference results of the fine mesh finite volume method (FVM). Copyright © 2000 John Wiley & Sons, Ltd.

KEY WORDS: Darcy porous media; dual reciprocity boundary element method; natural convection; primitive variables; thin plate splines

1. INTRODUCTION

Understanding the transport phenomena in porous media is of great importance in science and engineering. This interest appears to be increasing as a result of feasibility studies in diverse modern technologies, such as the use of geothermal energy in geology, secondary oil recuperation in petroleum engineering, disposal of radioactive wastes in nuclear engineering, fibrous insulation in mechanical engineering, powder metallurgy, and packed bed reactors in chemical engineering, to name but a few.

* Correspondence to: Laboratory for Fluid Dynamics and Thermodynamics, Faculty of Mechanical Engineering, University of Ljubljana, Aškerčeva 6, 1000 Ljubljana, Slovenia.

Received November 1998
Revised April 1999

Ever since the original work of Darcy [1] in 1856, the transport phenomena in porous media have been studied both experimentally and theoretically [2]. Despite the development of very sophisticated and relevant analytical techniques (see Reference [3]) a great majority of porous media models could be solved only by using discrete approximate solutions.

These solutions in parallel with the development of computers nowadays allow the evaluation of physically very complex situations. Moreover, the respective computational modeling gives an insight into the behavior of porous media in situations that are experimentally difficult, impossible, or too expensive to perform, e.g., see Goyeau *et al.* [4].

However, the diversity of the involved length scales, inhomogeneities, and anisotropies, together with the justification of using different classical models (Darcy, Brinkman, Forcheimer) in a specific situation, still represents a largely unresolved problem. An elaboration of the state-of-the-art in respective theoretical, experimental, and computational developments can be found in Kaviany [5].

A frequently encountered physical situation is the porous media natural convection problem, extensively treated by Nield and Bejan [6].

The problem of Darcy natural convection in porous media was first numerically studied by Chan *et al.* [7] in 1970, using the finite difference method (FDM) [8]. A similar study was performed approximately a decade late by Hickox and Gartling [9], using the finite element method (FEM) [10]. Prasad and Kulacki [11] pioneered the use of the fintie volume method (FVM) [12] for solving this problem.

The described natural convection problem represents, from the physical and computational points of view, a well-coped-with situation. However, the problem has not yet been solved by any of the boundary element method (BEM) techniques [13,14]. This fact is the principal motivation for the present research, in the sense of broadening the spectrum of physical situations for which the BEM might be used.

The BEM [15] is a weighted residual method for solving partial differential equations (PDEs), characterized by choosing an appropriate fundamental solution as a weighting function and by using the generalized Green's formula for the complete transfer of one or more partial differential operators to the weighted function. The main comparative advantage of the BEM over the discrete approximative methods is demonstrated in cases where this procedure results in the boundary integral equations only. This turns out to be possible only for some PDEs. In general, the procedure results in a boundary–domain integral equation. For example, when dealing with the BEM for the general transport equation structured by weighting with the fundamental solution of the Laplace equation, domain integrals appear at least from the transient, convective, and source terms.

The dual reciprocity boundary element method (DBREM) [16] represents one of the possibilities for transforming the resultant domain integrals into a finite series of boundary integrals. The key point of the DRBEM is the approximation of the field in the domain by a set of global approximation functions and subsequent representation of the domain integrals of these global functions by the boundary integrals. The discretization of the domain is respectively represented only by grid points (poles of the global approximation functions) in contrast to the FEM or FVM methods, where appropriate polygonization needs to be generated in addition. The DRBEM meshes thus in the domain resembling FDM meshes. However, the discretization of the geometry and fields on the boundary is piecewise polygonal,

which gives the method greater flexibility over the FDM methods in coping with the boundary quantities. In the DRBEM all calculations reduce to the evaluation of boundary integrals only. The mentioned DBREM characteristics might be advantageous in geometrically complex situations, which are often encountered in the context of porous media transport phenomena.

Despite the proven practical applicability of the DRBEM, important theoretical questions remain. For example, which global interpolation functions are most suitable for the representation of the fields in the domain, and where should the collocation points of these global interpolation functions be specified. Up to now both questions have been addressed mostly from the heuristic point of view. The most popular global intepolation function used in the majority of the DRBEM calculations in the field of transport phenomena so far are the conicals $1 + r_n$, with r_n representing the Euclidean distance between the field point $\mathbf{p}$ and a collocation point $\mathbf{p}_n$. The convergence of these functions was studied both numerically and in a more formal way [17]. To date, only *ad hoc* distributed points have been used, as an appropriate error estimator does not exist. Some mathematically substantiated answers to the first question have recently been discovered by Goldberg and Chen [18] in works concerning the theory of radial basis functions. It has been demonstrated [19] that the use of augmented thin plate spline radial functions gives an approximation that minimizes its curvature. The first theoretical investigations of the convergence of these functions were carried out in Reference [20]. An error and convergence analysis for the DRBEM for the Poisson equation have been recently reported by Goldberg *et al.* [21]. A typical example of a completely non-uniform DRBEM collocation point mesh in axis symmetry based on augmented thin plates splines [22] can be found in Reference [23].

The global interpolation of the fields over a domain introduces unknowns in the domain in addition to the unknowns at the boundary. The number of these additional unknowns usually exceeds the number of boundary unknowns. The systems of algebraic equations resulting from the DRBEM are thus large, fully populated, and asymmetric. A third important, but not sufficiently investigated aspect of the DRBEM method, is the possible iterative solution of associated systems of algebraic equations. This issue is of utmost importance when solving large-scale problems. Bulgakov *et al.* [24] have recently proposed two iterative solution techniques for DRBEM matrices originating from the diffusion equation.

The DRBEM for solving the energy transport equation was first applied to simple diffusion-governed linear [25] and non-linear problems [26], then to steady convective–diffusive problems [27], and finally successfully used in a completely non-linear transient convective–diffusive context, including phase-change effects and non-linearities arising simultaneously from material properties and boundary conditions [28,29].

The DRBEM for solving the steady state momentum transport equation in porous media was first demonstrated by El Harrouni *et al.* [30] through the use of the piezometric head variable and inhomogeneous permeability cast in hydraulic conductivity. Recently, the DRBEM was upgraded [31] for solving the related transient flow problem. In a later study, global interpolation functions of the type $1 + r_n$ as well $1 + r_n + r_n^2$ were used.

Very recently, Rahaim and Kassab [32] proposed a solution to coupled fluid flow and heat transfer problems by the DRBEM. However, they showed solutions based on $1 + r_n$ global approximation functions only for relatively simple unidirectional flow in a tube. The second principal motivation for the present research lies in assessing the suitability of the DRBEM

method in recirculating flow situations. For this purpose, a comparatively simple (no convection term, no diffusion term in the momentum equation) Darcy natural convection flow has been used as a logical starting point, which should lead to the treatment of more complicated fluid flow situations in the future.

The problem is solved as a weak non-linear coupled system of Poisson equations. Particular emphasis is placed on the integral representation of the pressure and temperature derivatives, principally differing from representation through global approximation functions used in Reference [32].

2. GOVERNING EQUATIONS

This paper deals with homogeneous porous media with porosity ϵ and permeability $\mathscr{K}$, confined to a two-dimensional domain Ω with boundary Γ. The rigid porous matrix and the incompressible fluid with viscosity μ saturating the pores have the same constant density ϱ, effective thermal conductivity k, and the specific heat at constant pressure c_p. The mass conservation for the defined system is

$$\nabla \cdot \mathbf{v} = 0 \tag{1}$$

where $\mathbf{v}$ stands for the seepage velocity. The momentum conservation is assumed to obey the Darcy law

$$0 = -\nabla P - \frac{\mu}{\mathscr{K}} \mathbf{v} + \mathbf{f} \tag{2}$$

with P denoting pressure and $\mathbf{f}$ the body force. The variation of the density with temperature is included through the body force term only by using the Boussinesq approximation

$$\mathbf{f} = \varrho \mathbf{a}(1 - \beta(T - T_{\text{ref}})) \tag{3}$$

with $\mathbf{a}$ denoting the acceleration vector, β the volumetric thermal expansion coefficient, T the temperature, and T_{ref} the reference temperature. The energy conservation equation is

$$\varrho c_p \nabla \cdot (\mathbf{v}T) = k \nabla^2 T \tag{4}$$

The solutions of Equations (1) and (2) are constructed by assuming impermeable velocity boundary conditions along the whole boundary Γ

$$\mathbf{v} \cdot \mathbf{n}_\Gamma = 0; \qquad \mathbf{p} \in \Gamma \tag{5}$$

where $\mathbf{n}_\Gamma$ denotes the normal on the boundary Γ, and $\mathbf{p}$ is the position vector. The solution of Equation (4) is constructed by assuming the division of the boundary Γ into not necessarily connected parts Γ^{D} and Γ^{N} with the Dirichlet and Neumann thermal boundary conditions respectively

$$T = T_\Gamma; \qquad \mathbf{p} \in \Gamma^D \tag{6}$$

$$-k \frac{\partial T}{\partial n_\Gamma} = F_\Gamma; \qquad \mathbf{p} \in \Gamma^N \tag{7}$$

where T_Γ and F_Γ represent known functions. The solution of the posed natural convection problem represents the velocity, pressure, and temperature distribution over the domain Ω and the boundary Γ.

3. SOLUTION PROCEDURE

3.1. Integral equations

The construction of the solution is represented in three steps. The first step involves the conversion of the PDEs into integral equations as well as basic elements of the iterative procedure. The second step focuses on the discretization and the last one on the setup and solution of the algebraic systems of equations.

The momentum equation is coupled with the energy equation through the body force. The energy equation is coupled with the momentum equation through the velocity field. Consequently, the solution inherently involves iterations. The solution steps are explained in a continuous setting, where no reference needs to be made regarding the discretization, which is explained afterwards.

Let us assume that the velocity, the pressure, and the temperature fields are all known at iteration level m. The discussion of the iteration cycle that follows explains how the velocity, pressure, and temperature fields are calculated at the next iteration level $m+1$.

The solution of the momentum equation at the iteration level $m+1$ is obtained in the following way.

The pressure Poisson equation (PPE) is constructed by taking the divergence of the momentum conservation (2)

$$\nabla^2 P^{m+1} = \nabla \cdot \left(-\frac{\mu}{\mathscr{K}} \mathbf{v}^m + \mathbf{f}^m \right) \tag{8}$$

For the assumed constant viscosity and permeability, the above equation reduces to

$$\nabla^2 P^{m+1} = \nabla \cdot \mathbf{f}^m \tag{9}$$

by taking into account the mass conservation equation (1). The Neumann pressure boundary conditions can be defined along the whole boundary Γ by taking the scalar product of the momentum equation with the normal on the boundary. This gives

$$\nabla P^{m+1} \cdot \mathbf{n}_\Gamma = \left(-\frac{\mu}{\mathscr{K}} \mathbf{v}^m + \mathbf{f}^m \right) \cdot \mathbf{n}_\Gamma; \qquad \mathbf{p} \in \Gamma \tag{10}$$

Since the impermeable velocity boundary conditions (5) are valid, the upper equation reduces to

$$\frac{\partial P^{m+1}}{\partial n_\Gamma} = \mathbf{f}^m \cdot \mathbf{n}_\Gamma; \qquad \mathbf{p} \in \Gamma \tag{11}$$

The PPE with the boundary conditions (11) is solved by weighting Equation (9) with the fundamental solution of the Laplace equation $T^*(\mathbf{p}; \mathbf{s})$ (where parameter $\mathbf{s}$ denotes the source point position) over the domain Ω. This gives the following integral equation after application of Green's second identity:

$$\int_\Gamma \frac{\partial P^{m+1}}{\partial n_\Gamma} T^* \, \mathrm{d}\Gamma - \int_\Gamma P^{m+1} \frac{\partial T^*}{\partial n_\Gamma} \mathrm{d}\Gamma - c_{\mathbf{s}}^* P_{\mathbf{s}}^{m+1} = \int_\Omega \nabla \cdot \mathbf{f}^m T^* \, \mathrm{d}\Omega \tag{12}$$

The superscript $\mathbf{s}$ denotes the evaluation of a quantity at the source point $\mathbf{s}$. $c_{\mathbf{s}}^*$ denotes the fundamental solution-related coefficient. The present paper is limited to the two-dimensional Cartesian system, e.g.

$$T^* = \frac{1}{2\pi} \log \frac{r_0}{r} \tag{13}$$

where r_0 represents the reference radius and r equals

$$r = \mathbf{r} \cdot \mathbf{r}; \qquad r = r_x \mathbf{i}_x + r_y \mathbf{i}_y; \quad r_x = p_x - s_x, \quad r_y = p_y - s_y \tag{14}$$

p_x, p_y denote the Cartesian co-ordinates (base vectors $\mathbf{i}_x$, $\mathbf{i}_y$) of point $\mathbf{p}$, and s_x, s_y the Cartesian co-ordinates of the fundamental solution source point $\mathbf{s}$ respectively.

Equation (12) is first used for determining the pressure distribution on the boundary Γ and subsequently explicitly in the domain Ω.

The pressure gradients on the boundary and in the domain can be explicitly calculated from the pressure gradient Poisson equation (PGPE)

$$\int_\Gamma \frac{\partial P^{m+1}}{\partial n_\Gamma} \nabla T^* \, \mathrm{d}\Gamma - \int_\Gamma P^{m+1} \nabla \frac{\partial T^*}{\partial n_\Gamma} \mathrm{d}\Gamma + \nabla (c_{\mathbf{s}}^* P_{\mathbf{s}}^{m+1}) = \int_\Omega \nabla \cdot \mathbf{f}^m \nabla T^* \, \mathrm{d}\Omega \tag{15}$$

obtained by taking the gradient of the PPE acting on the fundamental solution source point.

After calculating the pressure gradient field, the velocity field at iteration level $m+1$ can be explicitly calculated from the momentum equation

$$\mathbf{v}^{m+1} = \frac{\mathscr{K}}{\mu} \left(-\nabla P^{m+1} + \mathbf{f}^m \right) \tag{16}$$

The iteration cycle is completed by calculating the temperature field at iteration level $m+1$ (and with this also $\mathbf{f}^{m+1}$). This is accomplished by weighting the energy conservation equation by the fundamental solution of the Laplace equation and by using Green's second identity

$$\int_\Gamma \frac{\partial T^{m+1}}{\partial n_\Gamma} T^* \, d\Gamma - \int_\Gamma T^{m+1} \frac{\partial T^*}{\partial n_\Gamma} d\Gamma - c_s^* T_s^{m+1} = \int_\Omega \frac{1}{\alpha} \nabla\cdot(\mathbf{v}^{m+1} T^{m+1}) T^* \, d\Omega \tag{17}$$

with $\alpha = k/(\varrho c_p)$ denoting thermal diffusivity. Equation (17), together with the thermal boundary conditions (6) and (7), is used to simultaneously solve the unknown temperature distribution in the Neumann part of the boundary, the unknown temperature derivative in the normal boundary direction in the Dirichlet part of the boundary, and the unknown temperatures in the domain. The temperature gradients on the boundary and in the domain can be explicitly calculated from

$$\int_\Gamma \frac{\partial T^{m+1}}{\partial n_\Gamma} \nabla T^* \, d\Gamma - \int_\Gamma T^{m+1} \nabla \frac{\partial T^*}{\partial n_\Gamma} d\Gamma + \nabla(c_s^* T_s^{m+1}) = \int_\Omega \frac{1}{\alpha} \nabla\cdot(\mathbf{v}^{m+1} T^{m+1}) \nabla T^* \, d\Omega \tag{18}$$

obtained by taking the gradient of Equation (17) acting on the fundamental solution source point.

The iteration cycle is completed with the calculation of the updated body force

$$\mathbf{f}^{m+1} = \varrho \mathbf{a}(1 - \beta(T^{m+1} - T_{\text{ref}})) \tag{19}$$

The iterations are stopped when conditions

$$\begin{aligned} \left|\mathbf{v}^{m+1}\right| - \left|\mathbf{v}^m\right| &< v_\epsilon \\ \left|T^{m+1}\right| - \left|T^m\right| &< T_\epsilon \end{aligned} \tag{20}$$

are satisfied with v_ϵ and T_ϵ representing the velocity and temperature convergence criterions. In the case when iteration conditions (20) are not satisfied, a new iteration cycle starts with the relaxed value of the body force

$${}^{m+1}\mathbf{f} = {}^{m}\mathbf{f} + c_{\text{rel}}({}^{m+1}\mathbf{f} - {}^{m}\mathbf{f}) \tag{21}$$

with c_{rel} representing the heuristic relaxation factor. The discretization of the involved boundary–domain integral equations and respective formation of the algebraic equation systems for the solution of the unknowns is elaborated in below.

3.2. Discretization

The velocity, pressure, and temperature fields are all calculated on the same grid points $\mathbf{p}_n$; $n = 1, 2, \ldots, N$; $N = N_\Gamma + N_\Omega$. The first N_Γ grid points are distributed on the boundary and the last N_Ω in the domain. Two simple discretization alternatives are used to approximate the boundary integrals in Equations (12), (15), (17), and (18). The boundary geometry is approximated by N^Γ straightline segments, and the spatial variation of the fields on each of the boundary segments is represented by constant interpolation functions, with grid points coinciding with the geometrical centers of the straightline segments or with linear interpolation

functions with the two grid points standing symmetrically with respect to the geometrical centers of the straightline segments. In the constant case, $N_\Gamma = N^\Gamma$, and in the linear case, $N_\Gamma = 2N^\Gamma$. The Einstein summation convention is used in this text, i.e., any index that is repeated twice in a product is summed up. An underlined index is not summed up. This for boundary integrals of a scalar valued function $\mathscr{F}$, which in the present context denotes pressure or temperature, gives

$$\int_\Gamma \frac{\partial \mathscr{F}}{\partial n_\Gamma} T_l^* \, \mathrm{d}\Gamma - \int_\Gamma \mathscr{F} \frac{\partial T^*}{\partial n_{\Gamma l}} \, \mathrm{d}\Gamma - c_{\underline{l}}^* \mathscr{F}_l \approx G_{lk} \delta_{ki} \frac{\partial \mathscr{F}_i}{\partial n_\Gamma} - H_{lk} \delta_{ki} \mathscr{F}_i - c_{\underline{l}}^* \delta_{li} \mathscr{F}_i \tag{22}$$

where $k = 1, 2, \ldots, N_\Gamma$ and $i, l = 1, 2, \ldots, N$. Index l denotes $\mathbf{s}_l = \mathbf{p}_l$. δ represents the Kronecker symbol. Matrix elements G_{lk} and H_{lk} are defined as follows:

$$G_{lk} = \int_{\Gamma(k)} \Phi_k T_l^* \, \mathrm{d}\Gamma, \qquad H_{lk} = \int_{\Gamma(k)} \Phi_k \frac{\partial T_l^*}{\partial n_\Gamma} \delta\Gamma \tag{23}$$

where $\Gamma(k)$ and Φ_k represent the boundary segment and the boundary field shape function associated with the boundary grid point $\mathbf{p}_k$, and c_l^* is equal to

$$c_l^* = 0, \quad \mathbf{s}_l \notin \Omega \cup \Gamma; \qquad c_l^* = \frac{1}{2}, \quad \mathbf{s}_l \in \Gamma; \qquad c_l^* = 1, \quad \mathbf{s}_l \in \Omega \tag{24}$$

The shape functions in the local boundary element co-ordinate system $-1 \le \phi \le 1$ are equal to

$$\Phi = 1 \tag{25}$$

for constant elements and

$$\Phi_- = \frac{1}{2}\left(1 - \frac{\phi}{\underline{\phi}}\right)$$

$$\Phi_+ = \frac{1}{2}\left(1 + \frac{\phi}{\underline{\phi}}\right) \tag{26}$$

for linear elements, with $-1 \le \underline{\phi} \le 1$ measuring the relative position of the two boundary element grid points with respect to the geometrical center of the boundary element [33].

The domain integrals in Equations (12) and (17) are transformed by considering the approximation of the spatial variation of the fields in Ω by the global interpolation functions of the form

$$\mathscr{F}(\mathbf{p}) \approx \psi_u(\mathbf{p}) \varsigma_u, \quad u = 1, 2, \ldots, N + 3 \tag{27}$$

Two-dimensional scaled augmented thin plate splines are used in this work, due to theoretical considerations described in Reference [19].

$$\psi_n(\mathbf{p}) = r_n^2 \log r_n, \quad n = 1, 2, \ldots, N$$

$$\psi_{N+1}(\mathbf{p}) = p_x - p_x^0$$

$$\psi_{N+2}(\mathbf{p}) = p_y - p_y^0$$

$$\psi_{N+3}(\mathbf{p}) = 1$$

$$r_n^2 = (\mathbf{p} - \mathbf{p}_{\underline{n}})\cdot(\mathbf{p} - \mathbf{p}_{\underline{n}}) \tag{28}$$

The scaling constants p_x^0 and p_y^0 have been set to

$$p_x^0 = \frac{1}{2}(p_{x+} + p_{x-}), \qquad p_y^0 = \frac{1}{2}(p_{y+} + p_{y-}) \tag{29}$$

where p_{x+}, p_{y+} represent the maximum and p_{x-}, p_{y-} represent the minimum co-ordinates p_x, p_y respectively of the domain Ω.

Coefficients ς_u are calculated by constructing a system of $N+3$ algebraic equations

$$\boldsymbol{\Psi}\boldsymbol{\varsigma} = \mathscr{F} \tag{30}$$

The vectors are $\boldsymbol{\varsigma} = (\varsigma_1, \varsigma_2, \ldots, \varsigma_{N+3})^T$ and $\mathscr{F} = (\mathscr{F}_1, \mathscr{F}_2, \ldots, \mathscr{F}_N, 0, 0, 0)^T$. The first $v = 1, 2, \ldots, N$ rows of matrix $\boldsymbol{\Psi}$ are of the form $(\psi_{v1}, \psi_{v2}, \ldots, \psi_{vN+3})$, and the last three rows $v = N+1, N+2, N+3$ are of the form $(\psi_{1v}, \psi_{2v}, \ldots, \psi_{Nv}, 0, 0, 0)$, where the notation has been shortened to $\mathscr{F}_n \equiv \mathscr{F}(\mathbf{p}_n)$, $\psi_{nu} \equiv \psi_u(\mathbf{p}_n)$. Coefficients ς_u follow by inverting system (30)

$$\boldsymbol{\varsigma} = \boldsymbol{\Psi}^{-1}\mathscr{F} \tag{31}$$

Consequently, the domain integrals on the right-hand side of Equations (12) and (17) can be written in a compact dual reciprocity form ($k = 1, 2, \ldots, N_\Gamma$; $i, l = 1, 2, \ldots, N$; $u = 1, 2, \ldots, N+3$)

$$\int_\Omega \nabla\cdot\mathscr{G}T_l^* \, \mathrm{d}\Omega \approx \mathring{\Psi}_{,xlu}\Psi_{ui}^{-1}\mathscr{G}_{xi} + \mathring{\Psi}_{,ylu}\Psi_{ui}^{-1}\mathscr{G}_{yi} \tag{32}$$

with $\mathscr{G}$ denoting a vector-valued function with Cartesian components $\mathscr{G}_x$ and $\mathscr{G}_y$. The vector $\mathscr{G}$ is associated with body force in Equation (12) or with convection in the energy equation (17), and

$$\mathring{\Psi}_{,\xi lu} \equiv \int_\Omega \frac{\partial\psi_u}{\partial p_\xi} T_l^* \, \mathrm{d}\Omega \tag{33}$$

with ξ denoting x or y. The integral $\mathring{\Psi}_{,\xi lu}$ is calculated by defining the harmonic functions $\hat{\psi}_u$

$$\nabla^2 \hat{\psi}_u(\mathbf{p}) = \psi_u(\mathbf{p}) \tag{34}$$

which allows the integral to be represented as

$$\mathring{\Psi}_{,\xi lu} = \int_\Gamma \frac{\partial^2 \hat{\psi}_u}{\partial p_\xi \, \partial n_\Gamma} T^* \, \mathrm{d}\Gamma - \int_\Gamma \frac{\partial \hat{\psi}_u}{\partial p_\xi} \frac{\partial T^*}{\partial n_\Gamma} \, \mathrm{d}\Gamma - c^*_{\mathbf{s}} \frac{\partial \hat{\psi}_u(\mathbf{s})}{\partial p_\xi} \tag{35}$$

The upper boundary integrals are numerically evaluated by using the same discretization strategy that leads to expression (22)

$$\mathring{\Psi}_{,\xi lu} \approx G^{\psi}_{lk} \delta_{ki} \frac{\partial^2 \hat{\psi}_{iu}}{\partial p_\xi \, \partial n_\Gamma} - H^{\psi}_{lk} \delta_{ki} \frac{\partial \hat{\psi}_{iu}}{\partial p_\xi} - c^*_{\underline{l}} \delta_{li} \frac{\partial \hat{\psi}_{iu}}{\partial p_\xi} \tag{36}$$

However, matrices $\mathbf{G}^{\psi}$ and $\mathbf{H}^{\psi}$ could differ from matrices $\mathbf{G}$ and $\mathbf{H}$ because the boundary discretization that corresponds to the calculation of the fields on the boundary and integrals $\mathring{\Psi}_{lu}$ could differ in general. Let us denote the number of boundary grid points leading to the calculation of matrices $\mathbf{G}^{\psi}$ and $\mathbf{H}^{\psi}$ with N^{ψ}_{Γ}. Therefore, index k in Equation (36) runs as $k = 1, 2, \ldots, N^{\psi}_{\Gamma}$.

The adjacent harmonic functions $\hat{\psi}_u$ to the thin plate splines (28) are

$$\hat{\psi}_n = \frac{1}{16} r_n^4 \log r_n - \frac{1}{32} r_n^4$$

$$\hat{\psi}_{N+1} = \frac{1}{6} (p_x - p_x^0)^3$$

$$\hat{\psi}_{N+2} = \frac{1}{6} (p_y - p_y^0)^3$$

$$\hat{\psi}_{N+3} = \frac{1}{4} (p_x - p_x^0)^2 + \frac{1}{4} (p_y - p_y^0)^2 \tag{37}$$

The boundary integrals in Equations (15) and (16) are calculated as

$$\int_\Gamma \frac{\partial \mathscr{F}}{\partial n_\Gamma} \frac{\partial T^*_l}{\partial p_\zeta} \, \mathrm{d}\Gamma - \int_\Gamma \mathscr{F} \frac{\partial T^*}{\partial p_\zeta \, \partial n_{\Gamma_l}} \, \mathrm{d}T - c^*_{\underline{l}} \frac{\partial \mathscr{F}_l}{\partial p_\zeta} \approx G_{,\zeta lk} \delta_{ki} \frac{\partial \mathscr{F}_i}{\partial n_\Gamma} - H_{,\zeta lk} \delta_{ki} \mathscr{F}_i - c^*_{\underline{l}} \delta_{li} \frac{\partial \mathscr{F}_i}{\partial p_\zeta} \tag{38}$$

with ζ standing for x and y, and the matrix elements $G_{,\zeta lk}$ and $H_{,\zeta lk}$ are defined as follows:

$$G_{,\zeta lk} = \int_{\Gamma(k)} \Phi_k \frac{\partial T^*_l}{\partial p_\zeta} \, \mathrm{d}\Gamma, \qquad H_{,\zeta lk} = \int_{\Gamma(k)} \Phi_k \frac{\partial^2 T^*_l}{\partial p_\zeta \, \partial n_\Gamma} \, \mathrm{d}\Gamma \tag{39}$$

The domain integrals in Equations (15) and (18) are calculated as

$$\int_\Omega \nabla\cdot\mathscr{G}\,\frac{\partial T_l^*}{\partial p_\zeta}\,\mathrm{d}\Omega \approx \mathring{\Psi}_{,x\zeta lu}\Psi_{ui}^{-1}\mathscr{G}_{xi} + \mathring{\Psi}_{,y\zeta lu}\Psi_{ui}^{-1}\mathscr{G}_{yi} \tag{40}$$

with

$$\mathring{\Psi}_{,\xi\zeta lu} \equiv \int_\Omega \frac{\partial \psi_u}{\partial p_\xi}\frac{\partial T_l^*}{\partial p_\zeta}\,\mathrm{d}\Omega \tag{41}$$

Upper integrals are evaluated similar to those in Equation (36)

$$\mathring{\Psi}_{,\xi\zeta lu} \approx G^{\psi}_{,\zeta lk}\delta_{ki}\frac{\partial^2\hat{\psi}_{iu}}{\partial p_\xi\,\partial n_\Gamma} - H^{\psi}_{,\zeta lk}\delta_{ki}\frac{\partial\hat{\psi}_{iu}}{\partial p_\xi} - c^*_{\underline{l}}\delta_{li}\frac{\partial^2\hat{\psi}_{iu}}{\partial p_\xi\,\partial p_\zeta} \tag{42}$$

with index k running as $k = 1, 2, 3, \ldots, N_\Gamma^{\psi}$.

3.3. Systems of algebraic equations

After discretizing the boundary and transforming and discretizing the domain integrals in Equation (12) as described, the following compact form is obtained:

$${}_PC_{li}P_i^{m+1} + {}^PC_{li}\frac{\partial P^{m+1}}{\partial n_{\Gamma_i}} = {}_PC_l \tag{43}$$

with the coefficients

$${}_PC_{li} = -H_{lk}\delta_{ki} - c^*_{\underline{l}}\delta_{li} \tag{44}$$

$${}^PC_{li} = G_{lk}\delta_{ki} \tag{45}$$

$${}_PC_l = \mathring{\Psi}_{,xlu}\Psi_{ui}^{-1}f_{xi}^m + \mathring{\Psi}_{,ylu}\Psi_{ui}^{-1}f_{yi}^m \tag{46}$$

The terms ${}_PC_{li}$ and ${}^PC_{li}$ arise from the left-hand side and the term ${}_PC_l$ from the right-hand side of Equation (12). The application of the boundary conditions (5) yields the following system of N_Γ algebraic equations for calculating the pressure at the boundary:

$$\mathbf{A}^P\mathbf{x}^P = \mathbf{b}^P \tag{47}$$

with the system matrix $\mathbf{A}^P$ in the form

$$A_{li}^P = {}_PC_{li} \tag{48}$$

The vector of unknowns $\mathbf{x}^P$ is

$$x_l^P = P_l^{m+1} \tag{49}$$

and the adjacent right-hand side vector is

$$b_l^P = -{}^P C_{li}(f_{x\underline{i}}^m n_{\Gamma xi} + f_{y\underline{i}}^m n_{\Gamma yi}) + {}_P C_l \tag{50}$$

Pressure in the domain modes is calculated from the discrete analog of formula (12)

$$P_l^{m+1} = -\frac{1}{c_l^*}\left[\mathring{\Psi}_{,xlu}\Psi_{ui}^{-1} f_{xi}^m + \mathring{\Psi}_{,ylu}\Psi_{ui}^{-1} f_{yi}^m - G_{lk}\frac{\partial P^{m+1}}{\partial n_{\Gamma_k}} + H_{lk}P_k^{m+1}\right] \tag{51}$$

Similarly, the pressure gradient components at the boundary and in the domain nodes are calculated from the discrete analogue of formula (15)

$$\frac{\partial P^{m+1}}{\partial p_{\zeta_l}} = \frac{1}{c_l^*}\left[\mathring{\Psi}_{,x\zeta lu}\Psi_{ui}^{-1} f_{xi}^m + \mathring{\Psi}_{,y\zeta lu}\Psi_{ui}^{-1} f_{yi}^m - G_{,\zeta lk}\frac{\partial P^{m+1}}{\partial n_{\Gamma_k}} + H_{,\zeta lk}P_k^{m+1}\right] \tag{52}$$

After discretizing the boundary and transforming and discretizing the domain integrals in Equation (17) as described, the following compact form is obtained:

$${}_T C_{li} T_i^{m+1} + {}^T C_{li}\frac{\partial T^{m+1}}{\partial n_{\Gamma_i}} = 0 \tag{53}$$

with the coefficients

$${}_T C_{li} = -H_{lk}\delta_{ki} - c_{\underline{l}}^*\delta_{li} - \frac{1}{\alpha}\left[\mathring{\Psi}_{,xlu}\Psi_{u\underline{i}}^{-1} v_{xi}^{m+1} + \mathring{\Psi}_{,ylu}\Psi_{u\underline{i}}^{-1} v_{yi}^{m+1}\right] \tag{54}$$

$${}^T C_{li} = G_{lk}\delta_{ki} \tag{55}$$

The terms in the upper coefficients that involve $\mathring{\Psi}_{,\xi lu}$ came from the dual reciprocity transformation of the convective term. The others correspond to the diffusive term. The application of boundary conditions (6) and (7) yields the following system of N algebraic equations for calculating the unknown temperatures in the domain and the unknown temperatures or temperature derivatives at the boundary:

$$\mathbf{A}^T\mathbf{x}^T = \mathbf{b}^T \tag{56}$$

with the system matrix $\mathbf{A}^T$ in the form

$$A_{li}^T = \chi_{\underline{i}T} C_{li} + (1 - \chi_{\underline{i}})^T C_{li} \tag{57}$$

The vector of unknowns $\mathbf{x}^T$ is

$$x_i^T = \chi_{\underline{i}} T_i^{j+1} + (1 - \chi_{\underline{i}}) \frac{\partial T^{j+1}}{\partial n_{\Gamma_i}}, \quad i = 1, 2, \ldots, N_\Gamma \tag{58}$$

$$x_i^T = T_i, \quad i = N_\Gamma + 1, N_\Gamma + 2, \ldots, N \tag{59}$$

and the adjacent right-hand side vector, which involves the boundary conditions, is

$$b_l^T = -(1 - \chi_{\underline{i}})_T C_{li} T_{\Gamma i} - \chi_i{}^T C_{li}^F F_{\Gamma i} \tag{60}$$

The boundary conditions indicator χ_i is equal to 0 for $\mathbf{p}_i \in \Gamma^D \cup \Omega$ and equal to 1 for $\mathbf{p}_i \in \Gamma^N$. The temperature gradient components at the boundary and in the domain nodes are calculated from the discrete analogue of formula (18)

$$\frac{\partial T^{m+1}}{\partial p_{\zeta_l}} = \frac{1}{c_l^*} \left[\mathring{\Psi}_{,x\zeta lu} \Psi_{ui}^{-1} v_{x\underline{i}}^{m+1} T_{xi}^{m+1} + \mathring{\Psi}_{,y\zeta lu} \Psi_{ui}^{-1} v_{y\underline{i}}^{m+1} T_{yi}^{m+1} - G_{,\zeta lk} \frac{\partial T^{m+1}}{\partial n_{\Gamma_k}} + H_{,\zeta lk} T_k^{m+1} \right] \tag{61}$$

4. NUMERICAL EXAMPLES

4.1. Numerical implementation

The elements of the involved 12 boundary element matrices $\mathbf{G}$, $\mathbf{H}$, $\mathbf{G}^\psi$, $\mathbf{H}^\psi$, $\mathbf{G}_{,\xi}$, $\mathbf{H}_{,\xi}$, $\mathbf{G}_{,\xi}^\psi$, and $\mathbf{H}_{,\xi}^\psi$ are all calculated analytically. The corresponding formulas for the constant field shape function can be found in Reference [34] and the formulas for the linear shape functions will appear elsewhere. The evaluation of the hypersingular integral appearing in the matrices $\mathbf{H}_{,\xi}$ and $\mathbf{H}_{,\xi}^\psi$ when the collocation point coincides with the integration element is carried out in terms of the constant potential analogy in an internal harmonic function, with zero gradient in $\Omega + \Gamma$. The fundamental solution reference radius is set to $r_0 = 1$. The node position $\underline{\phi}$ is set to 2/3. The temperature and velocity iteration tolerances are set to $T_\epsilon = 10^{-4}$, $v_\epsilon = 10^{-4}$. The related criterion (20) is evaluated in all grid points. The involved systems of algebraic equations (30), (47) and (56) are, in the present work, solved by the standard subroutines from Reference [35]. The regular systems (30) and (56) are solved by lower–upper (LU) decomposition and back-substitution by using sub-routines LUDCMP and LUBKSB. System (47) is singular since the pressure is unknown up to an additive constant [36] in the posed pure Neumann problem. This system is thus solved by Householder reduction to bidiagonal form and QR diagonalization with shifts (see Reference [35], p. 469) by using sub-routines SVDCMP and SVBKSB. At this point it should be noted that intensive investigations are underway to solve systems (47) and (56) in an iterative way. The first contributions to this issue are described in Reference [24]. The DRBEM code has been coded in Digital Visual Fortran with double precision accuracy. Test cases have been run on a HP-Vectra 6/200 PC with an Intel Pentium Pro 200 MHz processor and 256 MB memory.

4.2. Differentially heated rectangular cavity

Consider a rectangular impermeable cavity $p_x^- \le p_x \le p_x^+ p_y^- \le p_y \le p_y^+$ with a heated boundary at $p_x = p_x^-$ and a cooled boundary at $p_x = p_x^+$. The boundaries at $p_y = p_y^-$ and the boundary at $p_y = p_y^+$ are insulated. The heated and the cooled boundaries are subject to Dirichlet boundary conditions

$$T_\Gamma(p_{x-}, p_y) = T^+ \tag{62}$$

$$T_\Gamma(p_{x+}, p_y) = T^- \tag{63}$$

The Neumann boundary conditions with $F_\Gamma = 0$ apply at both insulated boundaries

$$F_\Gamma(p_x, p_{y-}) = 0 \tag{64}$$

$$F_\Gamma(p_x, p_{y+}) = 0 \tag{65}$$

The posed classical natural convection problem can be written in a dimensionless form by defining the dimensionless co-ordinates $\tilde{p}_x$ and $\tilde{p}_y$

$$\tilde{p}_\xi = \frac{p_\xi - p_\xi^0}{\Delta p_\xi} \tag{66}$$

with $\Delta p_\xi = p_{\xi+} - p_{\xi-}$. Cavity height/width aspect ratio A is defined as

$$A = \frac{\Delta p_y}{\Delta p_x} \tag{67}$$

The dimensionless velocity $\tilde{\mathbf{v}}$ is defined as

$$\tilde{\mathbf{v}} = \frac{\Delta p_y}{\alpha} \mathbf{v} \tag{68}$$

The dimensionless pressure $\tilde{P}$ is defined as

$$\tilde{P} = \frac{\mathscr{K}}{\alpha\mu} P \tag{69}$$

The filtration Rayleigh number Ra^* based on cavity height is defined as

$$Ra^* = \frac{\varrho \mathscr{K} a \beta \Delta p_y \Delta T}{\alpha\mu} \tag{70}$$

with $\Delta T = T^+ - T^-$. The dimensionless temperature $\tilde{T}$ is defined as

$$\tilde{T} = \frac{T - T_{\text{ref}}}{\Delta T} \tag{71}$$

The Boussinesq reference temperature is set to $T_{\text{ref}} = \frac{1}{2}(T^+ - T^-)$. The dimensionless mass and momentum conservation equations are

$$\tilde{\nabla} \cdot \tilde{\mathbf{v}} = 0 \tag{72}$$

$$0 = -\tilde{\nabla} P - \tilde{\mathbf{v}} + Ra^* \tilde{T} \mathbf{i}_y \tag{73}$$

with the corresponding dimensionless boundary conditions

$$\tilde{\mathbf{v}} \cdot \mathbf{n}_\Gamma = 0 \tag{74}$$

The adjacent energy equation is

$$\tilde{\nabla} \cdot (\tilde{\mathbf{v}} \tilde{T}) = \tilde{\nabla}^2 \tilde{T} \tag{75}$$

with the corresponding dimensionless boundary conditions

$$\tilde{T}_\Gamma\left(\pm \frac{1}{2} A,\ \tilde{p}_y \right) = \pm \frac{1}{2} \tag{76}$$

$$\tilde{F}_\Gamma\left(\tilde{p}_x,\ \pm \frac{1}{2} \right) = 0 \tag{77}$$

The posed natural convection problem is completely defined through two dimensionless parameters, the aspect ratio A and the vertical filtration Rayleigh number Ra^*.

4.3. Reference solution

Since the analytical solution to the problem is not known, the characteristics of the developed method could be assessed only by comparing them with the solution obtained by some other numerical method. Surprisingly, the present authors have not found any fine-grid reference solution to the defined problem in the literature as, for example, exists for the natural convection of laminar Newtonian incompressible fluid in differentially heated rectangular cavity [37]. Instead, the FVM is used to generate a fine-grid reference solution to the governing equations. This discretization technique is well known, and a detailed description is not needed, only the main characteristics are presented hereinafter. Discrete temperature and pressure values are computed at the nodes of a computational grid defined on the two-dimensional rectangular domain, while the velocity components are calculated at the nodes of two staggered sub-grids. The conservation equations are integrated over the corresponding control volumes, leading to a local balance of the fluxes through the surfaces of the volume. The integrated equations are discretized, using a combination of the centered and upwind schemes, according to the value of the local mesh Péclet number (the hybrid scheme of

Patankar [12]). As the momentum equation is formulated in terms of the primitive variables (velocity and pressure), the iterative procedure includes a pressure correction calculation method to solve the pressure–velocity coupling. The code uses the classical simple technique [12] for the pressure and velocity correction. The set of linear discretized equations derived from each conservation equation is solved using an alternating direct implicit (ADI) procedure allowing for the use of the fast Thomas algorithm to solve tridiagonal equation systems. The convergence criterion is based on the average residue of the continuity equation on the whole domain and convergence is reached when this residue is less 10^{-7}.

The validation of the numerical code was performed over a large range of parameters for purely thermal natural convection in fluids [38,39] or in porous media. The numerical method was successfully used for solving double diffusive natural convection problems in fully [4] or partially [40] filled porous cavities, using the extended Brinkman formulation of the Darcy law.

The simulations presented hereinafter are based on the Darcy–Brinkman version of the code [4] using a very low Darcy number, $Da = 10^{-8}$.

The FVM calculations were performed on a Cray-C98 vector computer. An excellent level of vectorization of the code (95% of the execution in the vector mode) was obtained by vectorizing the tridiagonal equation system solver where most of the CPU time is spent.

4.4. Discussion of the result

The main purpose of the numerical test presented in this paper is to investigate the convergence and robustness of the developed method.

The DRBEM solution is compared with the reference values of overall cavity Nusselt number Nu^{ref} and streamfunction minimum $\psi_{\min}^{\mathrm{ref}}$ for the five sets of dimensionless parameters listed in Table I.

The following discretization errors are involved in the present DRBEM formulation: discretization error due to shape function representation of the fields on the boundary, discretization error due to global approximation of the fields in the domain, and discretization error that occurs by the boundary integral representation of the domain integrals of the global approximation functions. They interplay in the following characteristics of the developed method.

The DRBEM solution was compared with the reference solution by using seven meshes that are shown and explained in Figures 1(a)–(e) and 6(b) and (c). The corresponding isotherms

Table I. FVM reference solution for different aspect ratios and filtration Rayleigh numbers obtained by mesh consisting of $200 \times 200 = 40\,000$ grid points.

A	Ra^*	Nu^{ref}	$\psi_{\min}^{\mathrm{ref}}$
1.0	25	1.3682	−1.6550
0.5	50	2.1354	−2.1481
1.0	50	1.9794	−2.8633
2.0	50	1.3863	−2.6393
1.0	100	3.1018	−4.7357

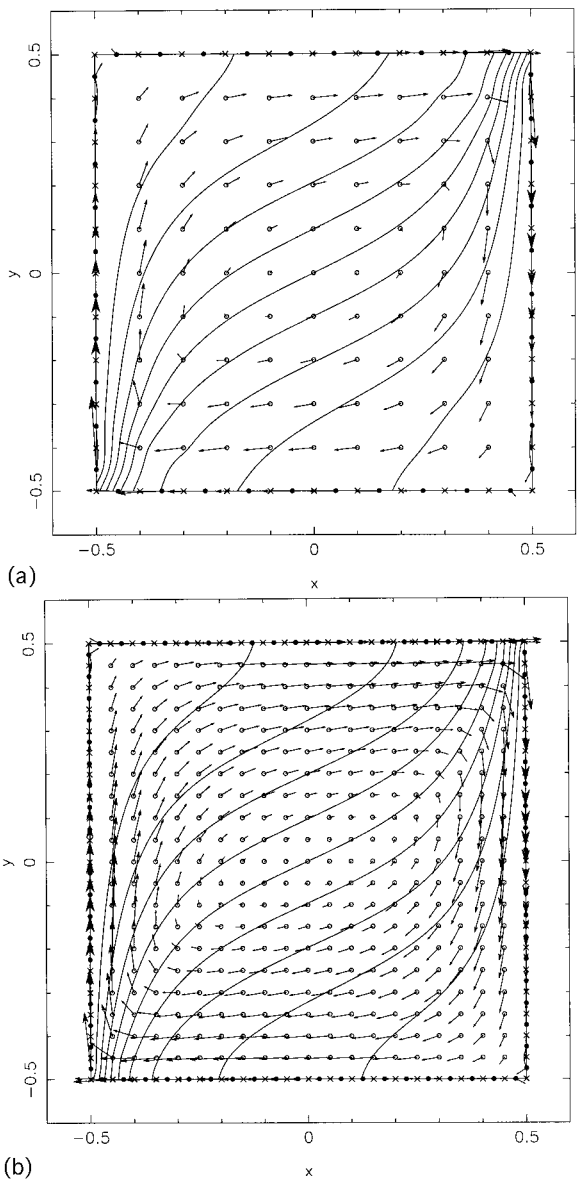

Figure 1. Isotherms and velocity vectors for $A = 1$, $Ra^* = 100$. (a), (b) and (c) discontinuous constant boundary elements; (d) and (e) discontinuous linear boundary elements. The boundary mesh points are represented with ●, the domain mesh points are represented with ○, and the borders between the boundary elements are represented with ×. Isotherms are equidistantly spaced. (a) Uniform mesh I (10×10) with $N_\Gamma = 40$, $N_\Omega = 81$, $N = 21$; (b) uniform mesh II (20×20) with $N_\Gamma = 80$, $N_\Omega = 361$, $N = 441$; (c) uniform mesh III (30×30) with $N_\Gamma = 120$, $N_\Omega = 841$, $N = 961$; (d) uniform mesh II/L with $N_\Gamma = 160$, $N_\Omega = 361$, $N = 521$; (e) non-uniform mesh II/LN with $N_\Gamma = 160$, $N_\Omega = 361$, $N = 521$. The length of the two neighboring boundary elements on one square side differs by 10%.

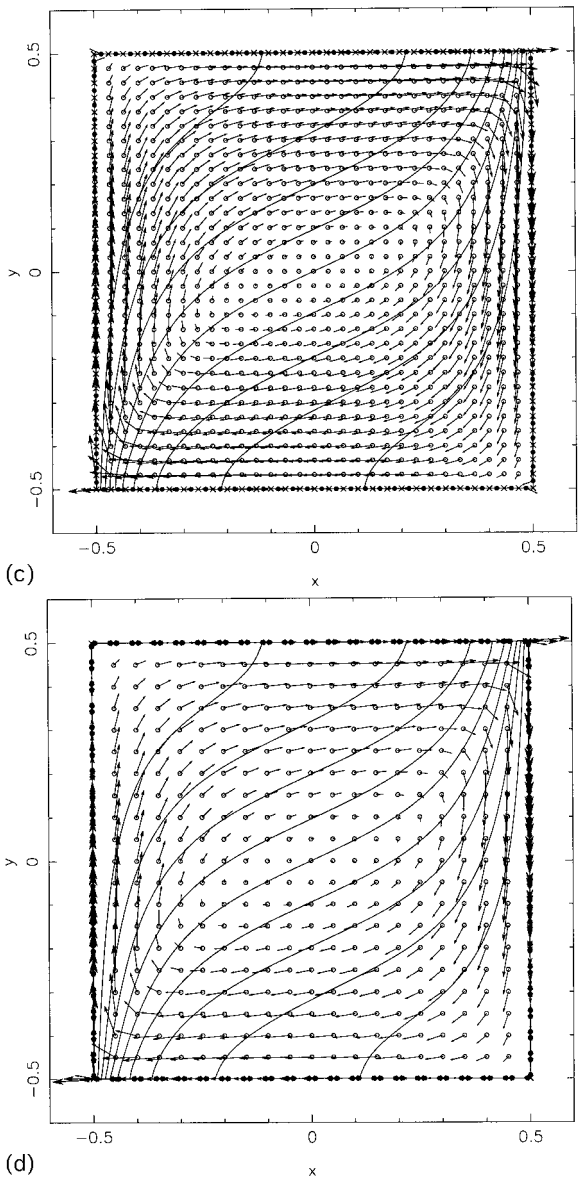

Figure 1 (*Continued*)

and velocity vectors are shown in Figure 1(a)–(e) for aspect ratio 1 and filtration Rayleigh number 100. All figures show the qualitative correctness of the temperature field. The non-permeable velocity boundary condition is not properly satisfied in solutions with constant

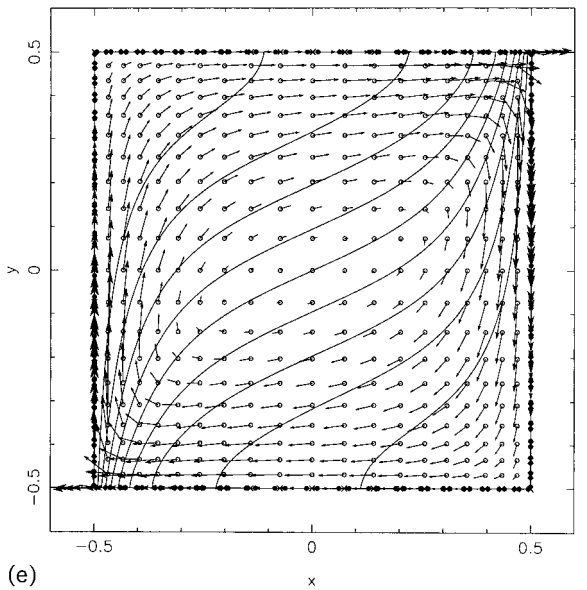

Figure 1 (*Continued*)

field shape function boundary elements, as shown in Figure 1(a)–(c). However, the flow across the boundary becomes less important with a finer mesh and localizes towards the corner. The solutions with the linear fields shape function boundary elements are shown in Figure 1(d) and (e) correctly represent the flow also in the corners. At this point a remark regarding the alternative calculation of the pressure derivatives in present formulation is appropriate. The pressure derivatives can be calculated from the pressure field in two different ways. The first one is through the integral representation formula (15) (PGPE). The second one is through the direct derivation of the global approximation representation (27) of the pressure field. The first procedure was chosen because of the tested superior accuracy over the second one; particularly regarding the satisfaction of the non-permeable boundary conditions.

Table II presents a comparison between the DRBEM solution and the reference solution in terms of the streamfunction minimum for the five different physical situations from Table I. The CPU times for solving the problem with $A = 1$, $Ra = 25$ with the Meshes I, II, and III are 7.5, 204.3, and 1693.3 s respectively on the PC platform defined in Section 4.1.

The results with $A = 1$, $Ra^* = 100$ and $c_{\text{ref}} = 1$ diverge, so c_{ref} is set to 0.1 for reaching convergence in this particular case. The number of required iterations to reach the solution grows with decreasing A and increasing Ra^*, as shown in Table II.

The relative difference in the calculated streamfunction minimum between the DRBEM calculations and the reference FVM solution for the five different physical situations is listed in Table I. It is below 1%, even for the most coarse mesh used. The comparison between the mid-plane velocity components depicted in Figures 2 and 3 for mesh I from Figure 1(a)

Table II. Accuracy of the DRBEM solution in terms of streamfunction minimum for different aspect ratios and filtration Rayleigh numbers as a function of meshing from Figure 1(a)–(e) and Figure 6(b) and (c).

Mesh	A	Ra^*	$\psi_{\min}$	$\Delta\psi'_{\min}$	$M_{\max}$	c_{rel}
I	1.0	25	−1.6417	−0.0080	9	1.0
II	1.0	25	−1.6424	−0.0076	9	1.0
III	1.0	25	−1.6424	−0.0076	9	1.0
I	1.0	50	−2.8586	−0.0016	18	1.0
II	1.0	50	−2.8526	−0.0037	18	1.0
III	1.0	50	−2.8507	−0.0044	18	1.0
I	1.0	100	−4.7808	+0.0095	83	0.1
II	1.0	100	−4.7257	−0.0021	85	0.1
III	1.0	100	−4.7168	−0.0040	85	0.1
II/L	1.0	100	−4.7163	−0.0019	85	0.1
II/LN	1.0	100	−4.7087	−0.0057	86	0.1
IV	0.5	50	−2.1409	−0.0026	30	1.0
V	2.0	50	−2.6263	−0.0049	10	1.0

$\Delta\psi'_{\min} = (\psi'_{\min} - \psi^{\text{ref}}_{\min})/\psi^{\text{ref}}_{\min}$, with $\psi^{\text{ref}}_{\min}$ listed in Table I. $M_{\max}$ represents the number of required iterations for reaching convergence with $\epsilon_T = 0.001$ and $\epsilon_v = 0.001$.

confirms this good agreement. The comparison of the related velocity solutions for other meshes used is not shown because the DRBEM solution completely coincides with the FVM.

Table III gives a comparison between the DRBEM solution and the reference solution in terms of the Nusselt number for the five different physical situations from Table I. The Nusselt number of the DRBEM solution is calculated in three different ways. The first one (denoted with subscript sng) originates from the direct calculation of the normal components of the temperature derivatives on the boundary from the equation system (56). The second one (denoted with subscript hyp) originates from the integral representation formula (18). The third one (denoted with subscript ψ) originates from the derivation of the global approximation representation (27) of the temperature field. Before commenting on the results from Table III showing the overall Nusselt numbers, a discussion on the local Nusselt number behavior is given. A comparison between the local Nusselt number at the heated boundary and the reference one is depicted in Figure 4(a)–(e) for the meshes from Figure 1(a)–(e). The Nu_{sng} results are physically incorrect (negative values!) at the top corner of the heated boundary for the constant field shape function boundary elements. This can be explained by the fact that such a primitive order of boundary element field shape functions [33] could not represent exactly the boundary heat flux, even in the limiting pure conduction-governed differentially heated cavity problem. However, the Nu_{hyp} and the Nu_{ψ} results are at least qualitatively correct with all meshes used. Table II clearly shows the convergence of the Nu_{ψ} towards the reference results with finer discretization (meshes I, II, III), with growing order of the approximation of the fields on the boundary elements (mesh II/L), and with the redistribution of the grid points towards the corners (mesh II/LN). Most accurate Nu number results are obtained in terms of Nu_{hyp} as shown in Table III.

Table III. Accuracy of the DRBEM solution in terms of Nusselt number for different aspect ratios and filtration Rayleigh numbers as a function of meshing from Figures 1 and 6.

Mesh	A	Ra^*	Nu_{sng}	Nu_{hyp}	Nu_{ψ}	ΔNu_{sng}	ΔNu_{hyp}	ΔNu_{ψ}
I	1.0	25	1.3748	1.3895	1.3358	+0.0048	+0.0156	−0.0237
II	1.0	25	1.3823	1.3910	1.3623	+0.0103	+0.0167	−0.0043
III	1.0	25	1.3830	1.3891	1.3698	+0.0108	+0.0153	+0.0017
I	1.0	50	1.9345	1.9804	1.8376	−0.0227	+0.0005	−0.0716
II	1.0	50	1.9735	2.0047	1.9253	−0.0030	+0.0128	−0.0273
III	1.0	50	1.9815	2.0041	1.9501	+0.0011	+0.0125	−0.0148
I	1.0	100	2.8997	3.1066	2.6106	−0.0652	+0.0016	−0.1584
II	1.0	100	3.0283	3.1301	2.8916	−0.0237	+0.0091	−0.0678
III	1.0	100	3.0678	3.1490	2.9864	−0.0110	+0.0152	−0.0372
II/L	1.0	100	3.0965	3.0976	3.0209	−0.0171	−0.0026	−0.0261
II/LN	1.0	100	3.0981	3.1039	3.0643	−0.0012	+0.0007	−0.0121
IV	0.5	50	2.1960	2.2280	2.1334	+0.0284	+0.0434	−0.0009
V	2.0	50	1.3847	1.3935	1.3763	+0.0012	−0.0052	−0.0052

$\Delta Nu = (\Delta Nu - \Delta Nu^{\mathrm{ref}})/\Delta Nu^{\mathrm{ref}}$, with Nu^{ref} listed in Table I. Subscripts sng, hyp, and ψ of Nu are explained in the text.

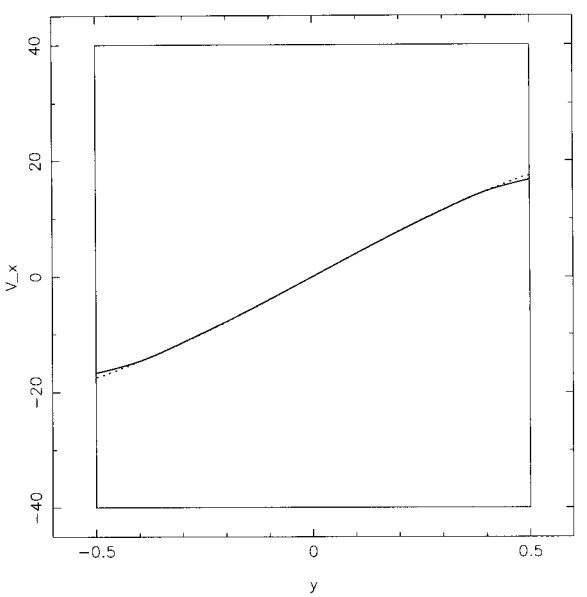

Figure 2. Dimensionless horizontal velocity $\tilde{V}_x$ at $\tilde{x} = 0$ as a function of cavity height for $A = 1$, $Ra^* = 100$ with mesh I from Figure 1(a). Dots represent the reference FVM solution in 198 grid points. The solid line represents the calculated global interpolation of the velocity component.

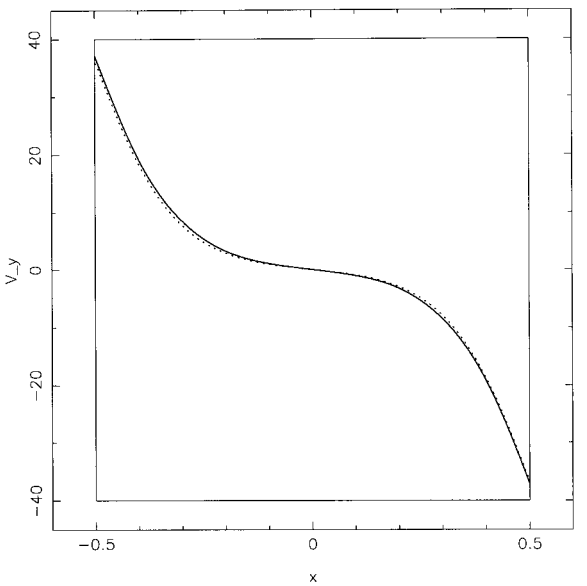

Figure 3. Dimensionless vertical velocity $\tilde{V}_y$ at $\tilde{y} = 0$ as a function of cavity width for $A = 1$, $Ra^* = 100$ with mesh I from Figure 1(a). The same symbols as in Figure 2.

Figure 5(a)–(e) shows the agreements between the DRBEM solution and the reference solution in terms of mid-plane temperature and lower insulated boundary temperatures for the meshes from Figure 1(a)–(e). The agreement between the mid-plane temperature results is good also for the very coarse mesh. The same observations regarding the DRBEM convergence of the local Nusselt number are valid also for the lower insulated boundary temperature convergence.

Figure 6(a)–(c) shows the calculated streamlines for $A = 1$, $Ra^* = 50$ and three different aspect ratios obtained by using the uniform meshes. The Nu_ψ and the streamfunction in this paper are calculated through the global approximation of the thermal and velocity fields. Related analytical expressions are summarized in Appendices A and B. Finally, it is important to point out that the calculations have been restricted to low Rayleigh numbers corresponding to a slow induced velocity field which is natural in porous media.

5. CONCLUSIONS

This paper describes the first attempt at solving the problem of Darcy natural convection in porous media by the BEM. Results are obtained for the rectangular cavities with aspect ratio 1/2, 1, and 2, and filtration Rayleigh numbers 25, 50, and 100. Discretization is based on the most simple geometrically straightline, constant, and linear field shape function boundary elements. The dual reciprocity transformation is based on augmented scaled thin plate splines.

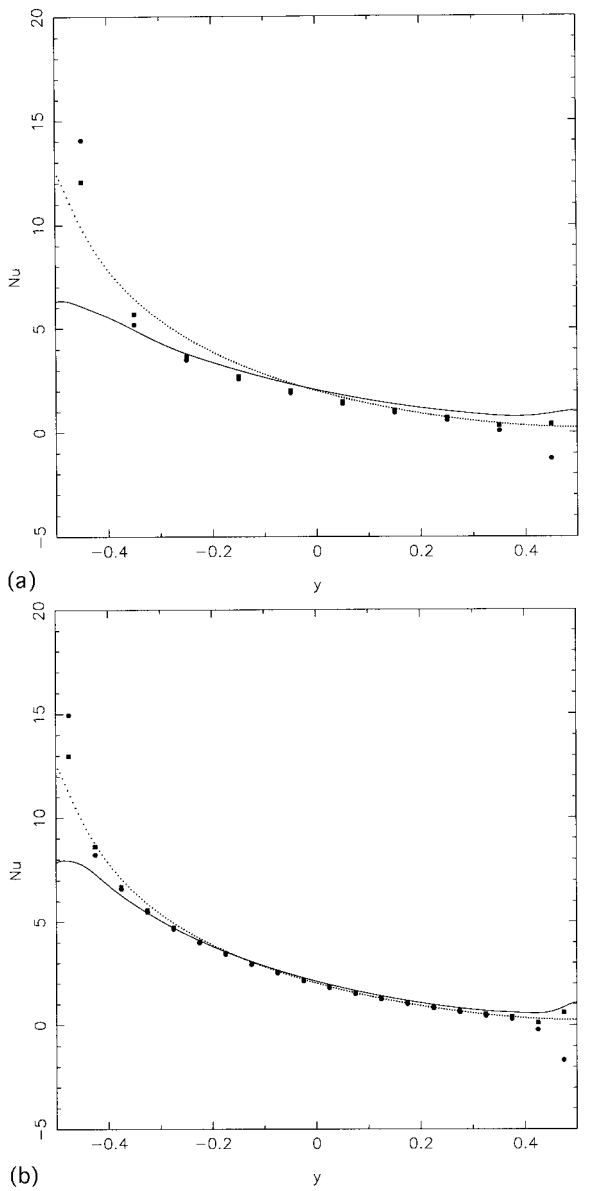

Figure 4. Hot side Nusselt number as a function of cavity height for $A = 1$, $Ra^* = 100$. Dots represent the reference FVM solution in 1998 grid points. Solid circles and squares represent the calculated local Nusselt number $Nu(p_y)$ in boundary grid points, evaluated from the boundary heat fluxes $Nu_{\mathrm{sng}}(p_y)$ and from the integral representation formula $Nu_{\mathrm{hyp}}(p_y)$ respectively. The solid line denotes the calculated $Nu_{\psi}(p_y)$ from the global interpolation representation of the heat flux. (a) Mesh I from Figure 1(a); (b) mesh II from Figure 1(b); (c) mesh III from Figure 1(c); (d) mesh II/L from Figure 1(d); (e) mesh II/LN from Figure 1(e).

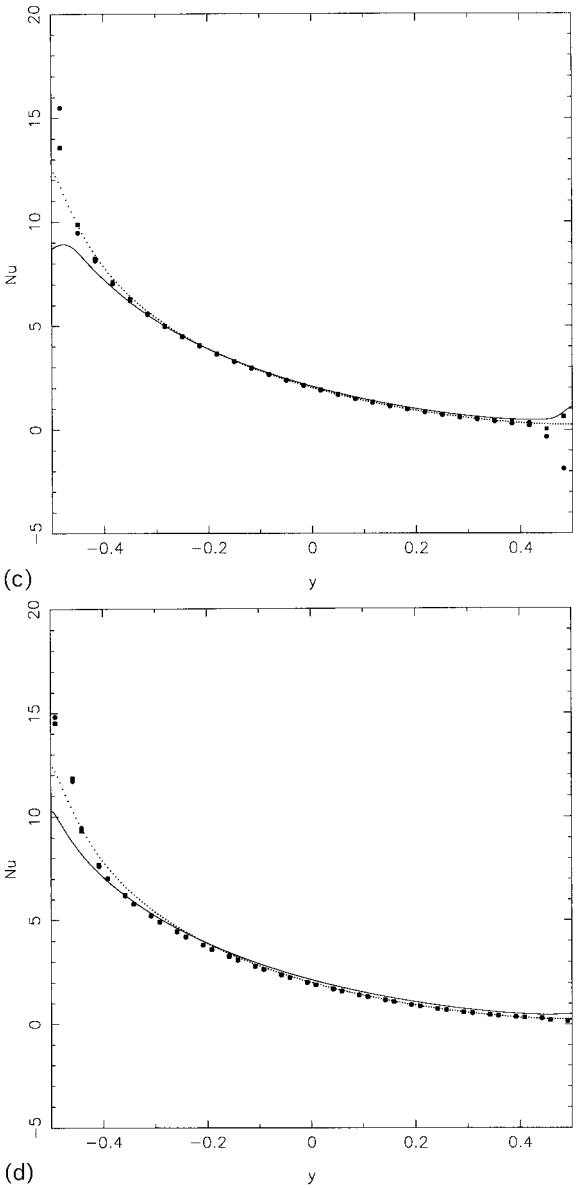

Figure 4 (*Continued*)

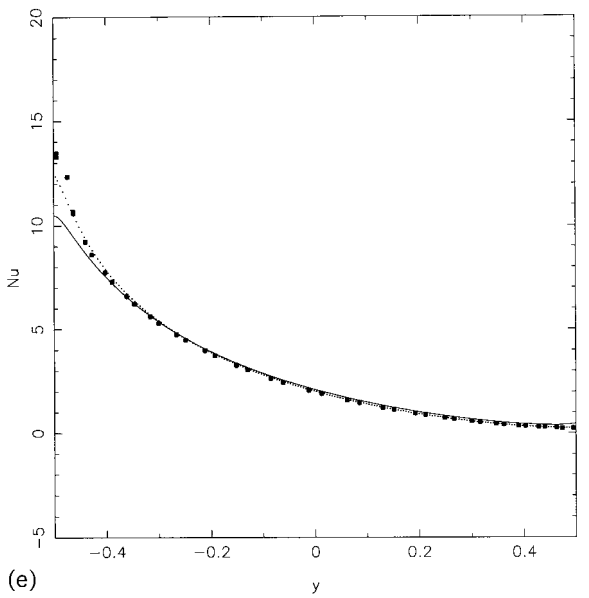

Figure 4 (*Continued*)

The solution is shown for uniform and non-uniform meshes. The described calculation of the temperature gradients and pressure gradients by the integral representation formula within the DRBEM context represents a completely new approach. This approach enables the calculation of the Nusselt number in three different ways of which the integral representation has been found to be most accurate. The calculation of the streamfunction and the Nusselt number from the global approximation representation of the fields leads to closed-form expressions as shown in the appendices.

It has been found that the physics of the problem are qualitatively properly described even with very coarse-mesh DRBEM results, which quantitatively do not differ substantially from the fine-mesh FVM values.

The results show convergence [41] of the h- (mesh refinement, compare results between meshes I, II, and III), p- (increased order of boundary field shape functions, compare results between meshes II and II/L), and r- (redistribution, compare results between meshes II/L and II/LN) types. The strength of the present method lies in accuracy, robustness, and in simple mesh structure, which can straightforwardly cope with geometrically complicated shapes. One drawback is the more complicated formulation of the solution procedure compared with the established numerical methods and the resulting full asymmetric matrices, which are difficult to solve in an economical way. It would be too ambitious to claim that the represented method could be extended to a wide variety of porous media situations in engineering practice at this point. Additional research is definitely required.

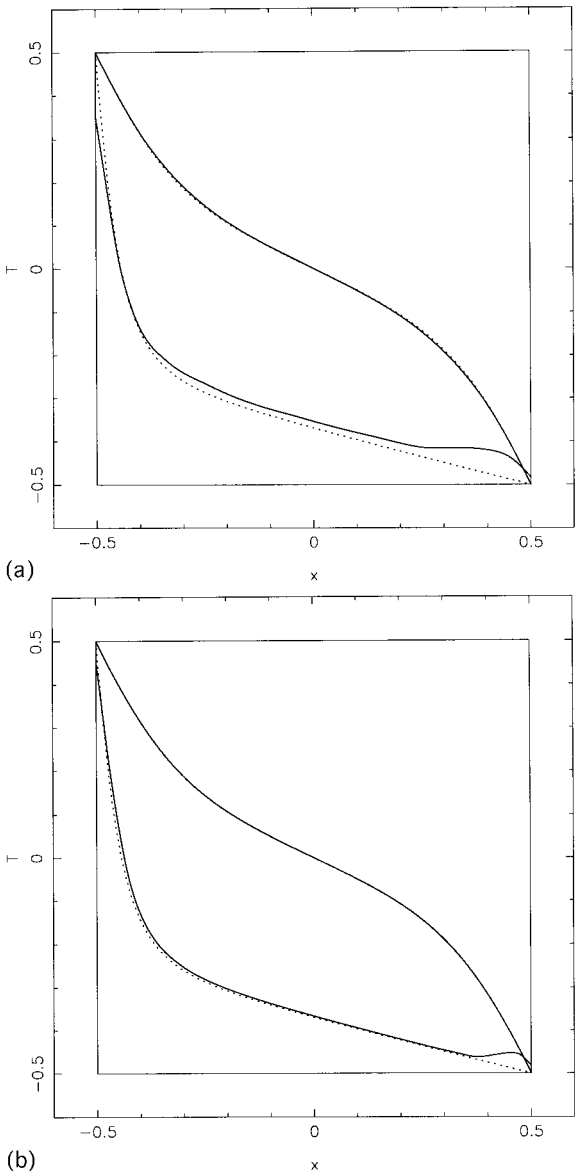

Figure 5. Dimensionless temperature $\tilde{T}$ at $\tilde{x} = x^-$ and $\tilde{x} = 0$ as a function of cavity width for $A = 1$, $Ra^* = 100$. Dots represent the reference FVM solution in 198 mesh points. The solid line represents the calculated global interpolation of the temperature. (a) Mesh I from Figure 1(a); (b) mesh II from Figure 1(b); (c) mesh III from Figure 1(c); (d) mesh II/L from Figure 1(d); (e) mesh II/LN from Figure 1(e).

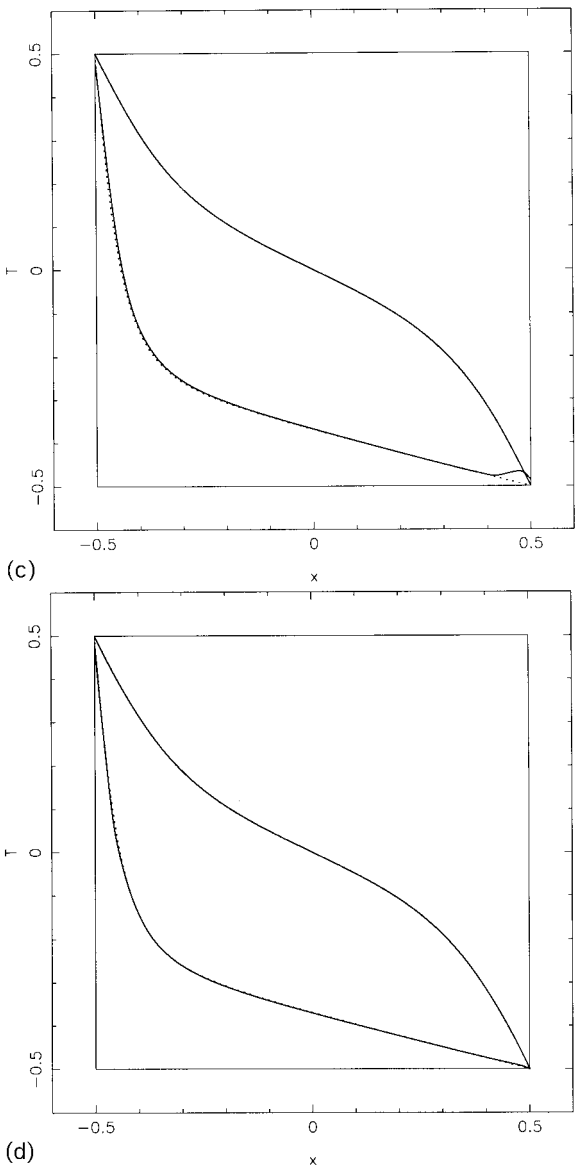

Figure 5 (*Continued*)

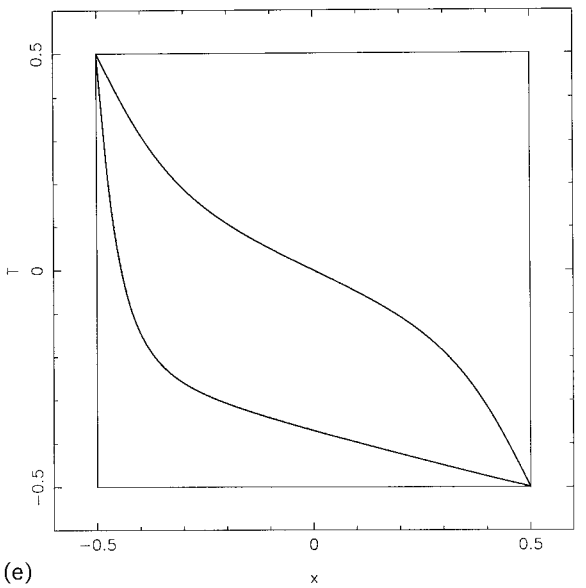

Figure 5 (*Continued*)

Therefore, our future efforts will be oriented towards physically more involved situations and towards numerical method improvements. In the first direction, solutions for higher Rayleigh number flows will be attempted, as well as solutions for inhomogeneous, anisotropic, and temperature-dependent materials, which frequently appear in practical problems. For this purpose, the proper corrections to the Darcy law will need to be made. Particularly interesting would be the extension to Darcy–Brinkman porous media, where the non-slip boundary conditions apply. The described principal solution procedure elements would most probably remain unchanged in such extensions. A formulation of the DRBEM solution for a physical model that involves temperature-dependent material properties and inhomogeneous permeability is shown in Reference [42]. Another interesting field-of-application for the present method are the external natural convection problems. In such cases, which might extend to infinity, another type of global interpolation functions that decay with r_n should replace the ones used in the present paper to properly match the far-boundary conditions. In the second direction, higher boundary elements will be numerically implemented and related analytical expressions developed. Since higher Rayleigh number flow situations require more dense meshes, the iterative solution of the relevant systems of algebraic equations would be of utmost importance. For this purpose, recently developed DRBEM iterative solvers [24] will be employed.

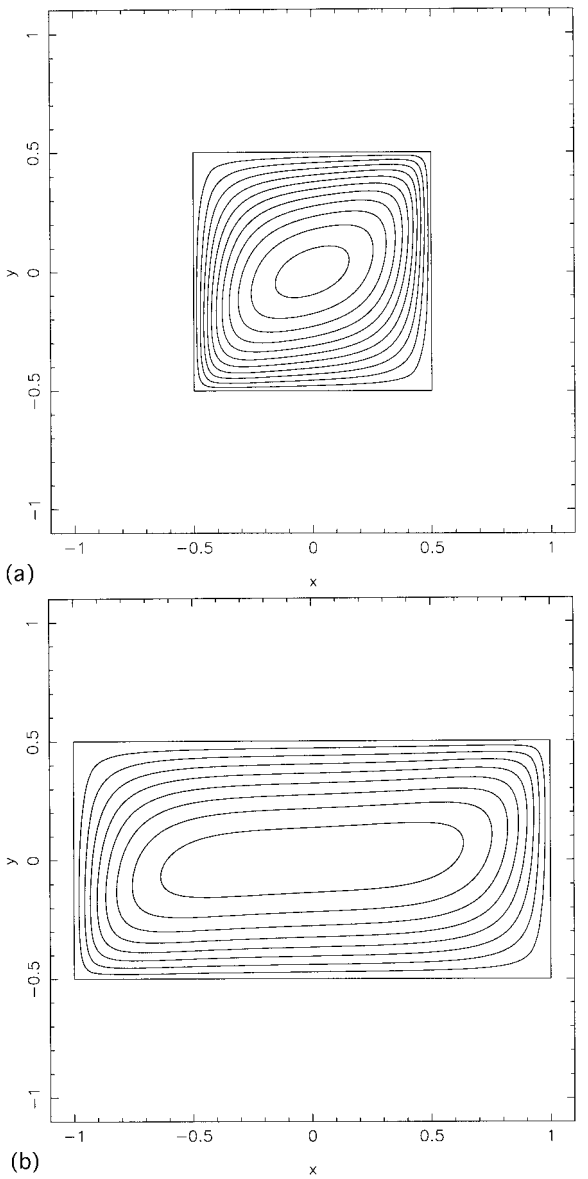

Figure 6. (a) Streamlines for $A = 1$, $Ra^* = 50$ with mesh III (20×20) from Figure 1(c). (b) Streamlines for $A = 1/2$, $Ra^* = 50$. Uniform mesh IV (40×20) with $N_\Gamma = 120$, $N_\Omega = 551$, $N = 671$. (c) Streamlines for $A = 2$, $Ra^* = 50$. Uniform mesh IV (20×40) with $N_\Gamma = 120$, $N_\Omega = 551$, $N = 671$. Discontinuous constant boundary elements for (b) and (c). All streamlines are equidistantly spaced with 0.25 step.

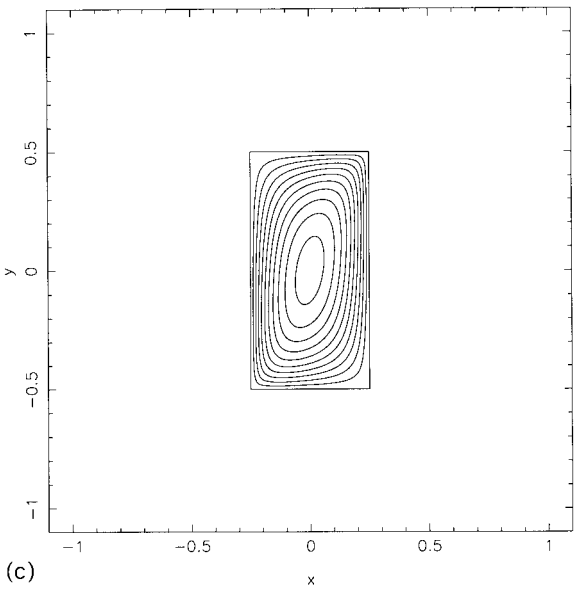

Figure 6 (*Continued*)

ACKNOWLEDGMENTS

The Slovenian and the French authors are grateful for the support provided through the bilateral French–Solvene Scientific Program CNRS-MZT. The English author is grateful for the support provided through the European Concerted Action COST3 P3: Simulation of Physical Phenomena in Technological Applications. The Slovenian authors would like to acknowledge the Slovenian Nuclear Safety Administration for financial support in the framework of the project 'Computational Modelling for Radionuclide Transport Estimation in Natural and Technological Systems'. The reference solutions calculations were performed on the Cray-C98 supercomputer of the CNRS at IDRIS (Orsay), under grant 0336 from the Engineering Sciences Department of the CNRS.

APPENDIX A. CALCULATION OF STREAMFUNCTION

The velocity–streamfunction ψ' relationship are

$$v_x = \frac{\partial}{\partial p_y}\psi'$$

$$v_y = -\frac{\partial}{\partial p_x}\psi' \tag{A1}$$

The streamfunction is calculated from the velocity components as

$$\psi' = \int_{p_y-}^{p_y} v_x \, \mathrm{d}p_y$$

$$\psi' = -\int_{p_x-}^{p_x} v_y \, \mathrm{d}p_x \tag{A2}$$

A variation of the velocity components over the domain Ω and boundary Γ is based on global approximation functions

$$v_x \approx \psi_n \Psi_{ni}^{-1} v_{xi}$$

$$v_y \approx \psi_n \Psi_{ni}^{-1} v_{yi} \tag{A3}$$

Respectively, the streamfunction could be calculated as

$$\psi' = \int_{p_y-}^{p_y} \psi_n \, \mathrm{d}p_y \, \Psi_{ni}^{-1} v_{xi}$$

$$\psi' = -\int_{p_x-}^{p_x} \psi_n \, \mathrm{d}p_x \, \Psi_{ni}^{-1} v_{yi} \tag{A4}$$

The involved intergrals over p_x are for $N = 1, 2, \ldots, N$ equal to

$$\begin{aligned}\int_{p_z-}^{p_x+} \psi_n \, \mathrm{d}p_x = {} & \frac{1}{3}\left[(p_{x+} \cdot (r_n(p_{x+})^2 + 2p_{ny}^2) \log r_n(p_{x+}) - p_{x-} \cdot (r_n(p_{x-})^2 + 2p_{ny}^2) \log r_n(p_{x-})\right] \\ & + \frac{2}{3} p_{yn}^3 \left[\arctan \frac{r_n(p_{x+})}{p_{yn}} - \arctan \frac{r_n(p_{x-})}{p_{yn}}\right] \\ & - \frac{1}{9}\left[(r_n(p_{x+})^2 - p_{yn}^2)^{1/2}(r_n(p_{x+})^2 - 5p_{yn}^2)\right. \\ & \left. - (r_n(p_{x-})^2 - p_{yn}^2)^{1/2}(r_n(p_{x-})^2 - 5p_{yn}^2)\right]\end{aligned} \tag{A5}$$

with

$$r_n(p_{x\pm}) = ((p_{x\pm} - p_{nx})^2 + (p_y - p_{ny})^2)^{1/2} \tag{A6}$$

The involved integrals over p_x are for ψ_{N+1}, ψ_{N+2}, ψ_{N+3} equal to

$$\int_{p_x-}^{p_x} \psi_{N+1} \, \mathrm{d}p_x = \frac{p_x^2 - p_{x-}^2}{2} - p_x^0 (p_x - p_{x-}) \tag{A7}$$

$$\int_{p_x-}^{p_x} \psi_{N+2} \, \mathrm{d}p_x = (p_y - p_y^0)(p_x - p_{x-}) \tag{A8}$$

$$\int_{p_{x-}}^{p_x} \psi_{N+3}\,\mathrm{d}p_x = p_x - p_{x-} \tag{A9}$$

The relationships for integrals over the p_y co-ordinate could be easily perceived from the given formulas for the integrals over the p_x co-ordinate and are thus not explicitly shown.

APPENDIX B. CALCULATION OF NUSSELT NUMBER

The local Nusselt number $Nu_\psi(p_y)$ is in the present work calculated as

$$Nu_\psi(p_y) = \frac{T_x(p_{x-}, p_y)}{A\Delta T} \tag{B1}$$

The overall cavity Nusselt number Nu_ψ in the present work is calculated as

$$Nu_\psi = \frac{\int_{p_{y-}}^{p_{y+}} T_x(p_{x-}, p_y)\,\mathrm{d}y}{A\Delta T} \tag{B2}$$

Variation of the temperature over the domain Ω and boundary Γ is based on global approximation functions

$$T_x(p_x, p_y) \approx \frac{\partial}{\partial p_x}\psi_n(p_x, p_y)\Psi_{ni}^{-1}T_i \tag{B3}$$

Respectively, $Nu_\psi(p_y)$ can be evaluated as

$$Nu_\psi(p_y) = \frac{(\partial/\partial p_x)\psi_n(p_{x-}, p_y)\Psi_{ni}^{-1}T_i}{A\Delta T} \tag{B4}$$

and Nu_ψ can be evaluated as

$$Nu_\psi = \frac{\int_{p_{y-}}^{p_{y+}} (\partial/\partial p_x)\psi_n(p_{x-}, p_y)\,\mathrm{d}p_y\Psi_{ni}^{-1}T_i}{A\Delta T} \tag{B5}$$

The involved integrals over p_y are for $n = 1, 2, \ldots, N$ equal to

$$\int_{p_{y-}}^{p_{y+}} \frac{\partial}{\partial p_x}\psi_n\,\mathrm{d}p_y = 2(p_x - p_{nx})\left[\frac{1}{2}(p_{y-} - p_{y+}) - (p_x - p_{nx})\right.$$
$$\left.\times \arctan\frac{p_x - p_{nx}}{p_{y+} - p_{ny}} - \arctan\frac{p_x - p_{nx}}{p_{y-} - p_{ny}} + (p_{y+} - p_{ny})\log r_n(p_{y+}) - (p_{y-} - p_{ny})\log r_n(p_{y-})\right] \tag{B6}$$

with

$$r_n(p_{y\pm}) = ((p_x - p_{nx})^2 + (p_{y\pm} - p_{ny})^2)^{1/2} \tag{B7}$$

The involved integrals over p_y are for $N+1$, $N+2$, and $N+3$ equal to

$$\int_{p_{y-}}^{p_{y+}} \frac{\partial}{\partial p_x} \psi_{N+1} \, \mathrm{d}p_y = p_{y+} - p_{y-} \tag{B8}$$

$$\int_{p_{y-}}^{p_{y+}} \frac{\partial}{\partial p_x} \psi_{N+2} \, \mathrm{d}p_y = 0 \tag{B9}$$

$$\int_{p_{y-}}^{p_{y+}} \frac{\partial}{\partial p_x} \psi_{N+3} \, \mathrm{d}p_y = 0 \tag{B10}$$

REFERENCES

1. Darcy H. *Les fontaines publique de la Ville de Dijon*. Victor Delmont: Paris, 1856.
2. Sahimi M. *Flow and Transport in Porous Media and Fractured Rock*. VCH: Weinheim, 1995.
3. Raghavan R, Ozkan E. *A Method for Computing Unsteady Flows in Porous Media. Pitman Research Notes in Mathematics Series*, vol. 318. Longman Scientific & Technical: Harlow, 1992.
4. Goyeau B, Songbe J-P, Gobin D. Numerical study of double-diffusive natural convection in a porous cavity using the Darcy–Brinkman formulation. *International Journal for Heat Mass Transfer* 1996; **39**: 1363–1378.
5. Kaviany M. *Principles of Heat Transfer in Porous Media*. Springer: Berlin, 1995.
6. Nield DA, Bejan A. *Convection in Porous Media*. Springer: Berlin, 1992.
7. Chan BKC, Ivey CM, Barry JM. Natural convection in enclosed porous media with rectangular boundaries. *Wärme Stoffübertragung* 1970; **7**: 22–30.
8. Bickley WG. Finite difference formulae for the square lattice. *Quarterly of Mathematical Applications in Mechanics* 1948; **1**: 35–49.
9. Hickox GE, Gartling DK. A numerical study of natural convection in a horizontal porous layer subjected to an end-to-end temperature difference. *Journal of Heat Transfer* 1981; **103**: 797–802.
10. Gartling DK, Hickox CE. *Mariah—A Finite Element Computer Program for Incompressible Porous Flow Problems*, *SAND79-1623*. Sandia National Laboratories, SAND77-1332: Albuquerque, NM, 1980.
11. Prasad V, Kulacki FA. Convection heat transfer in a rectangular porous cavity—effect of aspect ratio on flow structure and heat transfer. *Journal of Heat Transfer* 1984; **106**: 158–165.
12. Patankar SV. *Numerical Heat Transfer and Fluid Flow*. Hemisphere: New York, 1980.
13. Liggett JA, Liu PLF. *The Boundary Integral Equation Method in Porous Media Flow*. Allen & Unwin: London, 1983.
14. Power H, Wrobel LC. *Boundary Integral Methods in Fluid Dynamics*. Computational Mechanics Publications: Southampton, 1995.
15. Brebbia CA, Telles JCF, Wrobel LC. *Boundary Element Techniques; Theory and Application in Engineering*. Springer: Berlin, 1984.
16. Patridge PW, Brebbia CA, Wrobel LC. *The Dual Reciprocity Boundary Element Method*. Elsevier: London, 1992.
17. Yamada T, Wrabel LC, Power H. On the convergence of the dual reciprocity boundary element method. *Engineering Analysis* 1994; **13**: 291–298.
18. Golberg MA, Chen CS. The theory of radial basis functions applied to the BEM for inhomogeneous partial differential equations. *Boundary Elements Communications* 1994; **5**: 57–61.
19. Duchon J. Splines minimizing rotation invariant seminorms in Sobolev spaces. In *Constructive Theory of Functions of Several Variables. Lecture Notes in Mathematics*, vol. 571, Schemp W, Zeller K (eds). Springer: Berlin, 1997; 85–110.

20. Buhmann MD. Multivariate cardinal interpolation with radial basis functions. *Construction Approximates* 1990; **6**: 225–255.
21. Golberg MA, Chen CS, Bowman H, Power H. Some comments on the use of radial basis functions in the dual reciprocity method. *Computational Mechanics* 1998; **21**: 141–148.
22. Šarler B. Axisymmetric augmented thin plate splines. *Engineering Analysis* 1998; **21**: 81–85.
23. Šarler B, Mencinger J. Solution of temperature field in DC casted aluminium alloy billet by the dual reciprocity boundary element method. *International Journal for Numerical Methods in Heat and Fluid Flows* 1999; **3**: 269–295.
24. Bulgakov V, Šarler B, Kuhn G. Iterative solution of systems of equations in the dual reciprocity boundary element method for the diffusion equation. *International Journal for Numerical Methods in Engineering* 1998; **43**: 713–732.
25. Wrobel LC, Brebbia CA, Nardini D. The dual reciprocity boundary element formulations for transient heat conductions. In *Advances in Water Resources VI*, Sa da Costa A, Melo Baptista A, Gray WG, Brebbia CA, Pinder GF (eds). Springer: Berlin, 1986.
26. Wrobel LC, Brebbia CA. The dual reciprocity boundary element formulation for nonlinear diffusion problem. *Computational Methods and Applications in Mechanical Engineering* 1987; **37**: 262–282.
27. Wrobel LC, DeFigueredo DB. The dual reciprocity boundary element formulation for convection–diffusion problems with variable velocity fields. *Engineering Analysis* 1991; **8**: 312–319.
28. Šarler B, Kuhn G. Dual reciprocity boundary element method for convective–diffusive solid liquid phase change problems. Part 1: formulation. *Engineering Analysis* 1998; **21**: 53–63.
29. Šarler B, Kuhn G. Dual reciprocity boundary element method for convective–diffusive solid liquid phase change problems. Part 2: numerical examples. *Engineering Analysis* 1998; **21**: 65–79.
30. El Harrouni K, Quazar D, Wrobel LC, Brebbia CA. Dual reciprocity boundary element method for heterogeonous porous media. In *Betech VII*, Brebbia CA, Ingber MS (eds). London: Computational Mechanics Publications, Southampton and Elsevier, 1992; 151–159.
31. Eldho TI. A sensitivity study of transient groundwater flow using dual reciprocity boundary element method. In *BEM-XVIII*, Brebbia CA, Martins JB, Aliabadi MH, Haie N (eds). Computational Mechanics Publications: Boston, 1996; 637–646.
32. Rahalm CP, Kassab AJ. Pressure correction DRBEM solution for heat transfer and fluid flow in incompressible viscous fluids. *Engineering Analysis* 1996; **18**: 265–272.
33. Kythe PK. *An Introduction to Boundary Element Methods*. CRC Press: Boca Raton, FL, 1995.
34. Rek Z, Šarler B. Analytical integration of elliptic 2D fundamental solution and its derivatives for straight–line elements with constant interpolation. *Engineering Analysis* 1999; **23**: 515–525.
35. Press WH, Teukolsky SA, Vetterling WT, Flannery BP. *Numerical Recipes in Fortran*. Cambridge University Press: Cambridge, 1992.
36. Gresho PM, Sani RL. On pressure boundary conditions for the incompressible Navier–Stokes equations. *International Journal for Numerical Methods in Fluids* 1987; **7**: 111–145.
37. De Vahl Davis G, Jones IP. Natural convection in a square cavity: a comparison exercise. *International Journal for Numerical Methods in Fluids* 1983; **3**: 227–248.
38. Gobin D, Bennacer R. Cooperating thermosolutal convection in enclosure: 1. Scale analysis and mass transfer. *International Journal for Heat Mass Transfer* 1996; **39**: 2671–2681.
39. Gobin D, Bennacer R. Cooperating thermosolutal convection in enclosure: 2. Heat transfer and flow structure. *International Journal for Heat Mass Transfer* 1996; **39**: 2683–2697.
40. Goyeau B, Mergui S, Songbe J-P, Gobin D. Convection thermosolutale en cavite partiellement occupee par une couche poreuse faiblement permeable. *Comptes-Rendus de l'Académie des Sciences* 1996; **323**(II): 447–454.
41. Babuska I, Zienkiewicz OC, Gago J, Oliveira ER. *Accuracy Estimates and Adaptive Refinements in Finite Element Computations*. Wiley: Chichester, 1986.
42. Šarler B. Solid–liquid phase change in porous media: solution by boundary integral method. In *IABEM Symposium on Boundary Integral Methods for Nonlinear Problems*, Morino L, Wendland WL (eds). Kluwer Academic Publishers: Dordrecht, 1995; 185–190.

